Accepted Manuscript

Nanoparticle ζ-Potential Measurements using Tunable Resistive Pulse Sensing with Variable Pressure

James A. Eldridge, Geoff R. Willmott, Will Anderson, Robert Vogel

Please cite this article as: J.A. Eldridge, G.R. Willmott, W. Anderson, R. Vogel, Nanoparticle ζ-Potential Measurements using Tunable Resistive Pulse Sensing with Variable Pressure, *Journal of Colloid and Interface Science* (2014), doi: http://dx.doi.org/10.1016/j.jcis.2014.05.013

Nanoparticle ζ-Potential Measurements using Tunable Resistive Pulse Sensing with Variable Pressure

James A. Eldridge[a,b,c], Geoff R. Willmott[a,b,1,*], Will Anderson[d], Robert Vogel[e,f]

[a] Callaghan Innovation, 69 Gracefield Road, PO Box 31310, Lower Hutt 5040, New Zealand
[b] The MacDiarmid Institute for Advanced Materials and Nanotechnology, School of Chemical and Physical Sciences, Victoria University of Wellington, Wellington 6140, New Zealand
[c] School of Chemical and Physical Sciences, Victoria University of Wellington, Wellington 6140, New Zealand
[d] Centre for Biomarker Research and Development, Australian Institute for Bioengineering and Nanotechnology, The University of Queensland, Brisbane, Australia 4072
[e] School of Mathematics and Physics, The University of Queensland, Brisbane, Australia 4072
[f] Izon Science Limited, 8C Homersham Place, PO Box 39168, Burnside, Christchurch 8053, New Zealand

Abstract

Modern resistive pulse sensing techniques can be used to measure nanoparticle electrophoretic mobility, and hence ζ-potential. In contrast to conventional light scattering methods, resistive pulse sensing produces particle-by-particle data. We have used tunable resistive pulse sensing (TRPS) to compare methods for measuring the ζ-potential of carboxylated polystyrene nanoparticles. The five particle sets studied had nominal surface charge den-

---

*Corresponding author, g.willmott@auckland.ac.nz, Tel: +64 9 9239998

Email addresses: kaiwhata@gmail.com (James A. Eldridge), g.willmott@auckland.ac.nz (Geoff R. Willmott), will.anderson@uqconnect.edu.au (Will Anderson), robert@izon.com (Robert Vogel)

[1]Now at The Department of Physics, The University of Auckland, Private Bag 92019, Auckland, New Zealand

sity (σ) between 0 and -0.67 C m^{-2}, and diameters in the range 160 to 230 nm. Data were collected with pressure in the range ± 500 Pa applied across a tunable pore. In each experiment, pressure was varied either continuously or in discrete steps. Calculations of the ζ-potential were obtained by analysing both the rate and the full-width half maximum duration of resistive pulses. Data obtained from duration analyses were more reproducible than rate methods, yielding typical variations smaller than ± 5 mV. When σ was greater (less negative) than -0.32 C m^{-2}, all of the analysis methods studied yielded a monotonic relationship between ζ-potential and σ. Complicated pulse data were observed near the pressure at which the net particle flux is zero, and these observations have been explored by examining competition between electrokinetic and pressure-driven transport. The typical difference between ζ-potentials obtained using TRPS and phase analysis light scattering was 15% (< 5 mV), with an experimental error of $\sim 10\%$ attributable to both techniques.

1. Introduction

Measuring the ζ-potential of nanoparticles in solution is crucial for understanding and predicting the long-term stability of suspensions. Even in a well-characterised solution, it is difficult to accurately predict the ζ-potential from first principles [1]. Existing techniques for ζ-potential measurement draw upon either electrokinetic phenomena, such as electrophoretic light scattering or microelectrophoresis [2], or electroacoustic phenomena [3].

2

8 Such measurements are not trivial in nature, especially for relatively non-

9 uniform particle distributions, and they employ experimental procedures and

10 data analysis methods that can affect the ζ-potential value. The science of

11 nanoparticle ζ-potential measurement can be developed by studying mea-

12 surement consistency across different experimental conditions, apparatus and

13 analysis methods.

14 Resistive pulse sensing (RPS) can be used to measure the ζ-potential of

15 particles in solution based on their electrophoretic mobility. In RPS, an elec-

16 tric potential is used to drive ionic current through an electrolyte-filled pore

17 within an insulating membrane. If an insulating particle moves through the

18 pore, the resistance across the membrane is increased, producing a transient

19 decrease in measured current from the 'baseline' level, known as a resistive

20 pulse (Fig. 1(a)). Subsequent to development of this technique in Coulter

21 counters [4], DeBlois et al. [5] measured the electrophoretic velocity of virus

22 particles passing through polycarbonate pores, perhaps the first indication

23 that RPS could also be used for particle charge measurement. Nanoparticle

24 ζ-potentials have since been inferred from individual duration measurements

25 [6, 7]. More recent ζ-potential measurements [8–11] have considered resis-

26 tive pulses in much greater detail, accounting for multiple particle transport

27 mechanisms and conical pore geometry with end effects. Here we present a

28 detailed study and comparison of RPS-based ζ-potential measurement meth-

29 ods in which the rate or duration of resistive pulses is measured as a function

30 of applied pressure, with a view to optimising such techniques.

31 Our experiments employ a variant of RPS known as tunable RPS (TRPS),

32 in which the sensing pore is within an elastomeric membrane, which enables

3

33 nanoscale 'tuning' of the pore geometry by the symmetric application of

34 macroscopic stretch [11–14]. Tuning may be used, for example, to optimise

35 the signal-to-noise ratio [14], to sterically gate larger particles as the pore

36 diameter is reduced [14, 15], or to employ a single pore to investigate a wide

37 range of nanoparticle sizes [16]. Apart from charge, TRPS can be used to

38 measure nanoparticle size [17] and concentration [18]. Resistive pulse asym-

39 metry [19] and detection of aggregates or clusters [20] have been studied in

40 detail. The range of particles analysed using TRPS now includes dextran

41 particles [21], emulsions [9], liposomes and lyophilisomes [22–24], viruses and

42 bacteria [17, 25, 26], protein aggregates [27], exosomes and membrane vesicles

43 [28–31], expansile nanoparticles [16], magnetic beads [20, 32] and function-

44 alised gold nanoparticles [33]. DNA has been studied as both single molecules

45 [15] and on-bead [14, 21, 34, 35].

46   In this study, the ζ-potential of a particle ($\zeta_{particle}$) is measured by de-

47 termining its electrophoretic mobility in the Smoluchowski approximation,

48 in which particle size is much greater than the Debye length. Based on the

49 Nernst-Planck equation, significant contributions to particle flux through a

50 pore **J** can be summed as [17]

$$\frac{\mathbf{J}}{C} = \left(\frac{\varepsilon(\zeta_{particle} - \zeta_{pore})}{\eta} \right) \mathbf{E} + \frac{\mathbf{Q_p}}{A}. \tag{1}$$

51 Here C is the volume concentration of particles, ε and η are the fluid per-

52 mittivity and viscosity, and ζ_{pore} is the ζ-potential of the pore wall. **E** is the

53 applied electric field, A is the cross-sectional area of the pore, and $\mathbf{Q_p}$ is the

54 volumetric rate of pressure driven flow through the pore. Pressure-driven

55 flows in resistive pulse sensing have recently been studied elsewhere [36, 37].

4

56 Bulk transport via diffusion is typically negligible for TRPS [18], and it is

57 assumed that the gradient of the pore wall is shallow enough (on the length

58 scale of a particle) that the geometry can be considered locally cylindrical.

59 In experiments, we apply an external pressure across the fluid cell ($P_{applied}$),

60 and measure the value P_0 at which the transport mechanisms are balanced,

61 so that there is no net motion of particles through the pore ($\mathbf{J} = 0$), and

$$\zeta_{particle} = -\frac{\eta \mathbf{Q_P}}{\varepsilon \mathbf{E} A} - \zeta_{pore}. \tag{2}$$

62 To calculate $\zeta_{particle}$, a semi-analytical model has been developed ([8, 9], see

63 Supporting Information) to incorporate specific pore geometry, and therefore

64 to compute $\mathbf{E}$ and $\mathbf{Q_P}$ in terms of $P_{applied}$, the additional inherent pressure

65 within the fluid cell ($P_{inherent}$) and applied voltage (V). Independent electro-

66 osmotic flow experiments are used to characterise ζ_{pore}. Pores used for TRPS

67 exhibit conical geometry, which is modelled as indicated in Figure 1(b). The

68 small opening radius a, large opening radius b and length d are model inputs.

69 Vogel et al. [8] applied this method to a range of carboxylate polystyrene

70 nanoparticles, using TRPS with a custom built manometer to allow precise

71 control of $P_{applied}$. Somerville et al. [9] used the same technique to measure

72 the ζ-potential of a water-in-oil emulsion, and to explore the possibility of ζ-

73 potential measurements on individual particles. Relevant data have recently

74 been presented by Kozak et al. [11], who used essentially the same model of

75 tunable pores in calculations pertaining to the shape of individual pulses, and

76 by Weatherall et al. [38], who have used a similar but simpler calculation,

77 along with calibration particles of known ζ-potential in place of geometric

78 parameters. Here, we have collected further data for particles of various

5

79 sizes and surface charges. We aim to study the precision and accuracy of

80 the method used previously [8, 9], as well as three further methods which

81 identify P_0.

2. Materials and Methods

Table 1: Particle sets used in the present study. Diameters and surface charge details are as specified by the suppliers. Bangs Laboratories calculates charge densities as described in [39]. 'CO-psty' indicates carboxylated polystyrene.

Particle Set	Material	Manufacturer	Diameter	Charge density (σ)
			nm	C m^{-2}
A	Polystyrene	Polysciences	200	n/a[i]
B	CO-psty	Bangs	226	-0.181
C	CO-psty	Bangs	217	-0.318
D	CO-psty	Bangs	194	-0.400
E	CO-psty[ii]	Bangs	160	-0.666

[i] Particles are not carboxylated.

[ii] Surface groups include both carboxylic and polyacrylic acids.

83 The five particle sets studied, summarized in Table 1, consisted of four

84 sets of carboxylated polystrene (CO-psty) beads (Bangs Laboratories) and a

85 set of uncharged NIST traceable standards (Polysciences). All have diameter

86 close to 200 nm, but the nominal surface charge density (σ, determined from

87 titrations during manufacture) varies. Particles were suspended at concen-

6

88 trations of 10^9-10^{10} mL^{-1} in a standard electrolyte buffer (SEB) consisting of

89 0.1 M KCl, 15 mM 2-amino-2-hydroxymethyl-propane-1,3-diol (Tris), 0.01%

90 v/v Triton X-100 and 3 mM ethylenediaminetetraacetic acid (EDTA), ad-

91 justed to pH 8 using HCl. Prior to TRPS measurements, particles were

92 dispersed by vortexing for 5 s, sonicating at high power for 30 minutes and

93 passing through a 0.45 μm syringe filter (Minisart, purchased from Sigma-

94 Aldrich) to remove any remaining aggregates. Values of $\eta = 1.002$ mPa s

95 and $\varepsilon = 7.1$ x 10^{-10} C^2 N^{-1} m^{-1} were used in calculations ([40], for water

96 at 293 K). The Debye length (λ_D) of SEB is ~ 1.5 nm, and all particles and

97 pores in this study have minimum dimensions in excess of 100 nm, so the

98 Smoluchowski approximation ($\frac{a}{\lambda_D} \gg 1$) is valid.

99 TRPS was performed using the *qNano* system (Izon Science, described

100 in detail elsewhere [8, 12, 14, 15, 17–19]) which incorporates a fluid cell,

101 actuation capability for membrane tuning, and customised electronics. Here,

102 the high-precision customised manometer coupled to the fluid cell uses the

103 same principle and apparatus as in [8], but with the fluid flow to and from the

104 reservoir now controlled using a syringe pump (Cole-Parmer model 78961OC,

105 precise to 0.2 mL) fitted with 2 x 25 mL syringes (Terumo). The pressure

106 applied by the manometer to the fluid cell ($P_{applied}$) can be controlled with

107 precision better than ± 5 Pa (0.5 mm H$_2$0). The net pressure across the

108 membrane (P_{net}), equivalent to $P_2 - P_1$ (Fig. 1(b)), is the sum of the pressure

109 applied by the manometer ($P_{applied}$) and the pressure head within the cell

110 itself ($P_{inherent}$). When 40 μL of H$_2$O is loaded into the upper half of the

111 fluid cell, $P_{inherent}$ is 46 Pa (4.7 mm H$_2$O) [8].

112 Pore specimens are produced in thermoplastic polyurethane (TPU) by

7

113 mechanically puncturing a membrane using a chemically-etched tungsten
114 needle attached to an actuator [15]. Experiments were performed using a
115 pore specimen designated 'NP200' by the manufacturer (Izon Science), and
116 therefore most suitable for measurement of 200 nm particles. The stretch ap-
117 plied to the membrane was the same in all experiments so that any changes
118 in pore geometry were minimised [12]. To further mitigate possible geometric
119 changes or partial blockages, data were only collected when the baseline cur-
120 rent was within 10% of the average observed across all experiments. Based
121 on measurements using SEM, optical microscopy and a micrometer (see Sup-
122 porting Information), pore opening sizes (Fig. 1(b)) of $a = 184 \pm 20$ nm and
123 $b = 22.5 \pm 0.5$ μm were used in calculations, with a stretched membrane
124 thickness of $d = 179 \pm 7$ μm. Uncertainties primarily arise from measurement
125 resolution, variable application of stretch, and geometric non-idealities. The
126 uncertainty in absolute ζ-potential values due to pore geometry is ~ 30 %,
127 comparable to previous work [8]. This uncertainty applies to absolute values
128 of $\zeta_{particle}$, but not to comparative differences between particle sets measured
129 using the same pore. Pulses were identified and analysed using the *qNano*
130 system's proprietary software (v 2.2).

131 To find ζ_{pore}, electro-osmotic flow (EOF) measurements were performed
132 in microchannels that were custom-synthesized in pieces of the TPU used to
133 make pores (BASF Elastollan 1160D) using soft lithography. A laser direct
134 writer (Microtech 405A) produced a master channel (0.022 mm x 0.1 mm x
135 30 mm) in photoresist (MicroChem SU-8 2015) as described in [41]. Channels
136 were made using thermal embossing rather than using a bonding agent (as
137 used in [8]), which may chemically react with the polymer surface. EOF

8

138 measurements were performed using the current monitoring method [8, 42].
139 Channels were filled with SEB and a potential of 500 V was applied along the
140 channel length using silver electrodes. The value of ζ_{pore} used in calculations
141 was -11.4 mV, equal to the mean of 10 repeated measurements with the same
142 microchannel, with a standard deviation of 2.2 mV. After geometry, ζ_{pore}
143 generates the second greatest uncertainty for $\zeta_{particle}$ measurements. Details
144 of the embossing and results for variable KCl concentration are included in
145 the Supporting Information.

146 Comparative ζ-potential measurements were made using phase analysis
147 light scattering (PALS) with a Zetasizer Nano (Malvern). Immediately prior
148 to PALS measurements, particles suspended in SEB were sonicated for 5
149 minutes and passed through a 0.45 μm syringe filter to remove aggregates.
150 Each measurement was the mean value of 5 consecutive ζ-potential readings.
151 Following each set of 5 readings, the fluid cell was rinsed with deionised water
152 and reloaded with suspended particles. 3 of these measurements (15 readings)
153 were completed for each particle set. To prevent electrode oxidation, each
154 disposable fluid cell was replaced after 5 measurements (25 readings).

155 *2.1. Methods for Finding the ζ-Potential*

156 Four methods were used to analyse TRPS data for particle ζ-potential
157 measurement. In all methods, the strategy is to identify P_0 by collecting
158 resistive pulse data while controlling $P_{applied}$, the pressure applied to the
159 fluid cell. $P_{applied}$ can be varied continuously or in discrete steps. Exemplar
160 results from each method are presented in Fig. 2. The four methods involve
161 measurement of (a) continuous rate, (b) discrete rate, (c) continuous duration
162 and (d) discrete duration.

9

163   The continuous rate method has been described and used previously [8, 9].

164    $P_{applied}$ was continuously varied between +500 Pa and -500 Pa, ensuring that

165   resistive pulses were recorded in distinct regimes dominated by pressure-

166   driven flow, and by electrokinetics. The pressure was varied at 1.5 Pa s^{-1},

167   ensuring that a large number of pulses was counted and the chance of a

168   pore blockage during a measurement remained relatively low. P_0 is identified

169   as the pressure at which the net flow of particles through the pore is min-

170   imised. Figure 2(a) shows the cumulative pulse count with increasing $P_{applied}$,

171   producing an 'S'-shaped curve, and P_0 is determined by calculating the sta-

172   tionary point of a least-squares cubic fit to this curve. When the polarity of

173   the applied electric field is switched, P_0 changes because the direction of net

174   electrokinetic particle transport changes - the sign of $\mathbf{E}$ changes in Eq. 2. P_0

175   has been found using both continuously increasing and decreasing $P_{applied}$.

176   The discrete rate method (Fig. 2(b)) also identifies P_0 as the pressure at

177   which the minimum pulse rate occurs. In this case, the minimum is found by

178   fitting a parabola to discrete rate data. The impact of possible pore blockages

179   and the required measurement time are both reduced in comparison to the

180   continuous rate method. $P_{applied}$ was varied between +500 Pa and -500 Pa in

181   steps of 49 Pa (5 mm H$_2$O). Over 500 events were recorded at each $P_{applied}$

182   over a period of at least 30 s. Each measurement was visually inspected to

183   ensure that the rate was near-constant throughout the collection period, as

184   large deviations typically indicate a pore blockage.

185   The continuous duration method uses the full width half maximum (FWHM)

186   duration of pulse peaks to indicate the speed at which particles move through

187   the pore. P_0 is identified as the pressure at which the average FWHM is max-

10

188 imised due to the balance between the electrokinetic and pressure-driven

189 transport. The maximum duration is calculated by least squares fitting a

190 Gaussian function to FWHM data, obtained with pressure varied in the

191 same way as for the continuous rate method (above). A Gaussian function is

192 used because it is simple, symmetric about P_0, and accurately represents the

193 single-peak data obtained. Due to outliers (discussed further below), each

194 data point in Fig. 2(c) represents the mean of 5 consecutive FWHM mea-

195 surements. In the discrete duration method (Fig. 2(d)), data are collected

196 at discrete $P_{applied}$ values using the same regime as the discrete rate method.

197 As with the continuous duration method, the mean of a Gaussian fitted to

198 the data yields a measurement of P_0.

3. Results and Discussion

3.1. Pulse Rate Methods

201 P_0 data obtained using the continuous and discrete rate methods are

202 shown in Figure 3(a). Measurements were performed at both $V_0 = +0.5$

203 and -0.5 V, and corresponding values of P_0 are separated by the horizontal

204 line corresponding to $-P_{inherent}$, equivalent to $P_{net} = 0$. For typical values of

205 $\zeta_{particle}$ and ζ_{pore} in these experiments, the electro-osmotic and electrophoretic

206 transport mechanisms drive particles in opposite directions, but electrophore-

207 sis is larger. With positive applied voltage, particles are electrophoretically

208 driven towards the lower half of the fluid cell (Fig. 1(b)), so the opposing

209 pressure required for $\mathbf{J} = 0$ is negative. In the continuous case, each data

210 point represents two experiments, in which $P_{applied}$ was either increased or

211 decreased over time. The typical variation in P_0 between these cases was less

11

²¹² than 5%, and systematic variation is removed by plotting the average of the
²¹³ two values.

²¹⁴   All data sets show a monotonic trend with respect to nominal surface
²¹⁵ charge for the three data sets at $\sigma \geq$ -0.32 C m^{-2} (i.e. less negative than
²¹⁶ -0.32 C m^{-2}). The trend extends more weakly to particle set D ($\sigma =$
²¹⁷ -0.40 C m^{-2}). Particle set E ($\sigma = -0.67$ C m^{-2}) is exceptional, gener-
²¹⁸ ating widely varied P_0 measurements and resulting ζ-potential values. These
²¹⁹ observations, further discussed in Section 3.4, can be partly attributed to
²²⁰ the use of polyacrylic acid (in addition to carboxylate groups) to function-
²²¹ alise set E. Comparing continuous and discrete rate measurements, the trend
²²² with respect to surface charge is identical for $\sigma \geq$ -0.40 C m^{-2}. However, ab-
²²³ solute values of $P_0 - P_{inherent}$ are consistently smaller for the discrete rate
²²⁴ measurements.

²²⁵   Figure 3(b) plots ζ-potentials calculated from P_0 measurements in Fig. 3(a)
²²⁶ using Eq. 2 and experimental inputs from Section 2. The calculation accounts
²²⁷ for the polarity of V_0, so measurements at ± 0.5 V are treated as repeats. The
²²⁸ variability in these measurements is greatest for particle set E, giving unreli-
²²⁹ able data, and smallest for sets A and B. Consistent with Fig. 3(a), discrete
²³⁰ measurements give lower absolute values of $\zeta_{particle}$.

²³¹   Data obtained using PALS (Fig. 3(b)) agree with the TRPS data. Ig-
²³² noring particle set E, the average PALS value is close to the discrete and
²³³ continuous results, and consistently lies between them. The continuous rate
²³⁴ data are within experimental uncertainty of the PALS data, with maximum
²³⁵ differences of 4.6 mV (absolute) and 24% (fractional) across sets A-D. The
²³⁶ equivalent maximum differences for the discrete rate data are 8.3 mV and

12

237 29%. It is notable that $|\zeta_{particle}|$ is lower for particle set D than for set C in

238 three of the four data sets plotted. The exception to this trend [8] used the

239 same particle sets (A-D) in experiments.

240 The two key advantages of the rate methods are, firstly, that considerable

241 data obtained over a wide range of conditions are brought to bear on the task

242 of finding P_0, and secondly, that pulses do not need to be further analysed

243 once they have been identified. The primary difficulty with rate methods

244 is that pulses recorded within $\sim$50 Pa of P_0 are often non-ideal (further

245 discussed in Section 3.4), and identification of P_0 is strongly dependent on

246 these pulses. Previously [8] these issues have been partially mitigated by

247 discarding events within 50 Pa of P_0 prior to fitting.

248 In general, the continuous rate method offers more precision than the dis-

249 crete rate method. The latter method involves a trade-off between precision

250 and time per measurement, which is dependent upon the discrete step size.

251 The discrete raw data (Fig. 2) are smoother near P_0, but the parabolic fit

252 has uncertainty on a similar scale to the step size. The discrete method also

253 has advantages, namely that it is less vulnerable to spurious pulses near P_0,

254 it is not terminally interrupted when a pore blockage occurs, and it does not

255 require pressure changes in chronological sequence. For the continuous case,

256 the latter requirement can be mitigated by checking and averaging results

257 for increasing and decreasing pressures.

258 *3.2. Duration Methods*

259 Measurements of P_0 using duration methods are summarized in Fig. 4(a).

260 There are broad similarities to data obtained using the rate methods, such

261 as the division of P_0 values for different polarity of V_0 about the horizontal

13

262 line equivalent to $P_{net} = 0$. Again, P_0 monotonically increases with σ at

263 low absolute values, including particle set D (σ =-0.4 C m^{-2}), although

264 data for set E is again inconsistent. In contrast with Fig. 3(a), there is

265 no clear systematic difference (and indeed very good agreement) between

266 discrete and continuous data. Overall, $|P_0 - P_{inherent}|$ data are smaller than

267 those produced by the rate methods, and it is notable that these values are

268 greater at positive rather than negative values of V_0. These trends are further

269 explored in Section 3.4.

270 Calculated ζ-potentials with measurements at ± 0.5 V treated as repeats

271 (Fig. 4(b)) yield a monotonic relationship between σ and $\zeta_{particle}$, other than

272 for particle set E. The relatively large uncertainty in ζ-potentials for particle

273 sets C and D relative to sets A and B is a feature of both Figs. 3(b) and 4(b).

274 For these particle sets, $\zeta_{particle}$ values may have high dispersity, or random

275 measurement uncertainly may be relatively large for the specific measurement

276 parameters (including σ) used here.

277 The maximum difference between duration data and the corresponding

278 PALS data is 7.0 mV (absolute) or 25% (fractional) for sets A-D. Across these

279 four particle sets and all four methods (i.e. 16 measurements), the average

280 difference between TRPS and PALS $\zeta_{particle}$ values was 3.4 mV (absolute) or

281 15% (fractional). The average uncertainty attributed to repeated measure-

282 ment was 10% for the TRPS methods and 11% for PALS. PALS and rate

283 measurements (Fig. 3(b)) indicated a higher absolute ζ-potential for particle

284 set C than for set D, suggesting that values of σ (manufacturer-specified)

285 and $\zeta_{particle}$ may not be monotonically related. This trend was not observed

286 in Fig. 4(b), although as with the rate data, PALS results are consistent with

14

287 duration data for all particle sets A-D.

288   Overall, duration measurements of $\zeta_{particle}$ are more reproducible than
289 measurements using pulse rates. Figures 3(b) and 4(b) each contain data for
290 six individual measurements using each particle set (four measurements for
291 set B). When each set of six is treated as repeats, all five particle sets have a
292 lower coefficient of variation (equivalent to standard deviation as a fraction
293 of the mean) in the case of duration measurements.

294   As with the rate methods, the discrete duration method usually requires
295 less measurement time than the continuous method, but affords less preci-
296 sion depending on the discretization. Although pulses close to P_0 are again
297 problematic (naïvely, the FWHM tends to ∞ at P_0), each pulse is analysed
298 more closely than for the rate methods, resulting in less uncertainty. Nev-
299 ertheless, the Gaussian fit can be significantly affected by individual events,
300 and indeed it is prudent to partially discretise the continuous data by aver-
301 aging five consecutive individual events for each data point (Fig. 2). FWHM
302 pulse durations do not change greatly with pulse magnitude, the latter be-
303 ing proportional to particle volume [17]. For example, for a sample of set C
304 particles the pulse FWHM varied by < 14 % between the largest (1.3 nA)
305 and smallest (0.5 nA) pulses, corresponding to < 30 % variation in particle
306 diameter. The range of mean particle diameters for the sets used here was
307 $\sim$40% (Table 1). This could partly account for the low P_0 value for particle
308 set E.

3.3. Comparison of Methods

310   Figure 5 summarizes ζ-potential measurements using TRPS, plotting the
311 difference between the value for each method and the mean value over all

15

312 methods. Duration measurements, both continuous and discrete, are always

313 within $\pm \sim 5$ mV of the mean, further indicating that duration measurements

314 produce more precise (self consistent) results than event rate methods. Oc-

315 casional variations closer to 10 mV are obtained using the rate methods, es-

316 pecially for more highly charged particles. For particles of unknown charge,

317 there is clear advantage in taking measurements using multiple TRPS tech-

318 niques to check for self consistency, and to avoid measurements such as those

319 found to be characteristic of highly charged particles here.

320 Some of the trends observed in Figs. 3 and 4 are further evident in Fig. 5.

321 The continuous and discrete rate data lie either side of the mean in all cases,

322 due to the consistently lower absolute values of $\zeta_{particle}$ derived from discrete

323 measurements. The continuous rate data point for particle set C appears

324 here to be an outlier with low reproducibility. This demonstrates how the in-

325 consistent trend observed for sets C and D in Fig. 3, discussed above and sup-

326 ported by PALS data, could originate from measurement uncertainty rather

327 than from characteristics of the actual particle distribution. The possibility

328 of measurement error in the nominal charge densities (Table 1) should also

329 be noted.

330 Although the rate methods depend on pulses near P_0 (Section 3.1), the

331 analysis required for these methods is relatively facile, requiring only accurate

332 identification of each event. In comparison, duration measurements employ a

333 detailed analysis of each individual event. This provides advantages, such as

334 the ability to discard individual events if they are considered to be outliers,

335 and the possibility to extract more information from each individual event.

336 Indeed, $\zeta_{potential}$ can in principle be calculated from a single event, without

16

337 variable pressure [11]. However, the model is designed for an ideal particle

338 travelling smoothly along the central pore axis, and so for individual particle

339 charge measurements factors such as off-axis trajectory, steric interactions

340 and polydispersity should be considered. The comparison between continu-

341 ous and discrete methods can be summarized by noting that the precision

342 of discrete data is limited by the discrete step size, but that discretization

343 allows flexibility over the step size as well as timing and quality control of

344 measurements.

3.4. Highly Charged Particles

346   In Section 3.1, the high variability of P_0 data and derived ζ-potentials for

347 particle set E (Figs. 3 and 4) was partly attributed to differences in functional

348 groups. In addition, set E has the highest nominal charge of the particle

349 sets used (Table 1), which may give rise to complications due to competing

350 flow effects near the pore constriction, at the smaller opening (Fig. 1(b)).

351 Figure 6 employs the semi-analytic model used above for ζ-potential calcula-

352 tions to plot the relative contributions to particle transport for a specific set

353 of experimental parameters. Due to the differences between electrokinetic

354 and pressure driven flows, the dominant transport mechanism can switch

355 within (say) a few tens of nanometers of the geometric discontinuity at the

356 pore opening, causing the particle flux to change sign. Additionally, parti-

357 cle transport varies across the width of the pore [32]. The pressure-driven

358 flow profile is approximately parabolic (as in Poiseuille flow), while electro-

359 osmosis is nearly a plug flow, and electrophoresis depends on the electric field

360 geometry. This consideration of transport details reveals that complexities

361 in particle transport will not be captured by Eqs. 1 and 2.

17

362   Figure 6 shows that particle transport can be asymmetric about the pore

363 constriction. In this example, any on-axis particle near the small pore open-

364 ing (on either side) will be transported away from the pore, potentially cre-

365 ating a region of depleted particle concentration around the pore opening.

366 Particles approaching the constriction from above the membrane move differ-

367 ently to those moving from within the pore. This asymmetry could explain

368 differences between P_0 magnitudes (relative to $P_{inherent}$) for positive and neg-

369 ative applied voltages, which are especially evident for duration method data.

370   Perhaps more importantly, competing mechanisms produce a higher like-

371 lihood of abnormal resistive pulses near P_0 due to steric or Brownian mecha-

372 nisms. Abnormal pulses (see Supporting Information for an example) can be

373 generally characterized as those caused by particle lingering near the pore,

374 perhaps passing through multiple times, rather than cleanly passing through.

375 In our experiments, competition between pressure-driven and electrokinetic

376 transport is increased when particles have high charge. There is also greater

377 range of $P_{applied}$ at which abnormal pulses were observed, although this could

378 also be caused by relatively high polydispersity. As demonstrated in Figure 7,

379 fitting of a cubic to the continuous rate method can be uncertain under these

380 conditions, with multiple possible inflection points observed. The accuracy

381 of P_0 measurement is similarly uncertain for particle set E.

382   Possible differences between P_0 for the cases of $\mathbf{J} = 0$ and maximised

383 duration could explain why ζ-potentials are consistently smaller when ob-

384 tained by the duration methods, in comparison with the rate methods. As

385 identified in rate experiments, P_0 is the pressure at which the number of

386 particles passing through the constriction is minimised. This may differ from

18

387 the pressure at which the average particle flux is zero, because it is possible
388 for particles to be moving through the pore in both directions, promoted
389 by transport variation across the pore width. As for maximised duration,
390 the dominant transport mechanism acting on a particle can vary as it moves
391 along the z-axis on length scales comparable to the size of the particle.

392 This Section reveals clear directions for future improvement of TRPS-
393 based particle charge measurement methods. A significant step would be to
394 establish a process to identify (and discard) abnormal pulses, and draw upon
395 event asymmetry [19] to establish the direction of particle motion through
396 the pore. Research into the importance of precise pore geometry and com-
397 petition between transport mechanisms will be ongoing. The convergence
398 of the electric field at the pore constriction may give rise to significant DC
399 dielectrophoresis. Further work is required to establish the working range
400 of particle charge measurements for pores of different sizes and in different
401 electrolytes.

4. Conclusion

403 We have studied variable pressure methods for ζ-potential measurement
404 using TRPS. Measurements are comparable to PALS data between zero sur-
405 face charge and -0.4 C m^{-2}, both in terms of absolute values and repeatabil-
406 ity. Use of tunable pores enables multiple measurement and analysis meth-
407 ods, an advantage over light scattering. Key advances in this paper include
408 introduction and comparison of four relatively simple analysis techniques,
409 improved experimental control, and more rigorous determination of ζ_{pore} (a
410 key parameter for $\zeta_{particle}$ calculation). Our results are more reproducible

19

when calculations are based on FWHM duration data than when rate data are used. Collection of data over a range of experimental conditions has ensured that uncertainties are clear. Uncertainty increased for more highly charged particles due to competing electrokinetics and pressure about the pore opening. Future work should focus on measurement uncertainties due to pore geometry and surface charge parameters used in calculations. TRPS charge measurements could also be extended to a wider range of particles. Transport of larger particles is readily dominated by pressure-driven flows, so low-conductivity electrolyte and modified electronics should be used to allow the application of larger voltages necessary to measure electrokinetic transport.

Acknowledgements

20
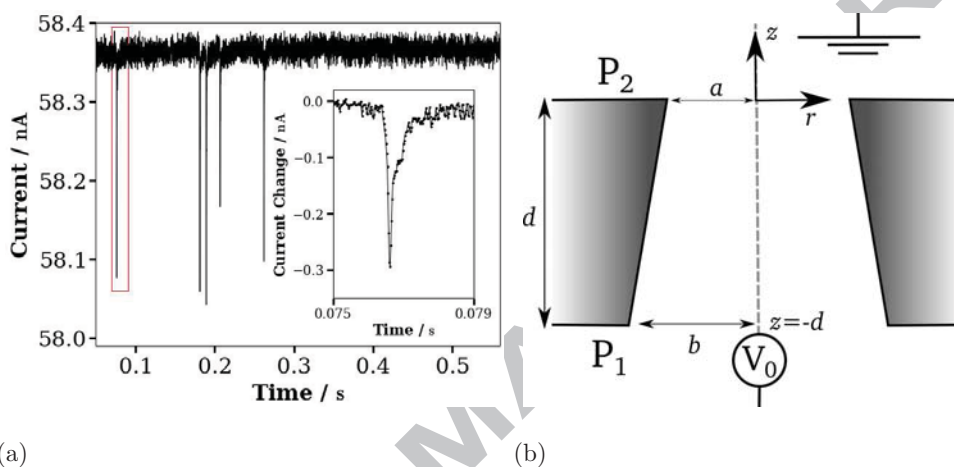
(a)   (b)

Figure 1: (a) shows typical tunable resistive pulse events. Each downwards pulse in current from the baseline level indicates that a 200 nm carboxylated polystyrene sphere (from set C, Table 1) has passed through the pore constriction. Inset, an expansion of the red outlined region. Events are asymmetric because pores are near-conical in shape. (b) is a schematic section of a tunable pore, showing the truncated conical pore geometry with small and large pore openings a and b respectively, the membrane thickness d, and the cylindrical polar co-ordinates (r, z). The net pressure across the membrane is $P_{net} = P_2 - P_1$.

21
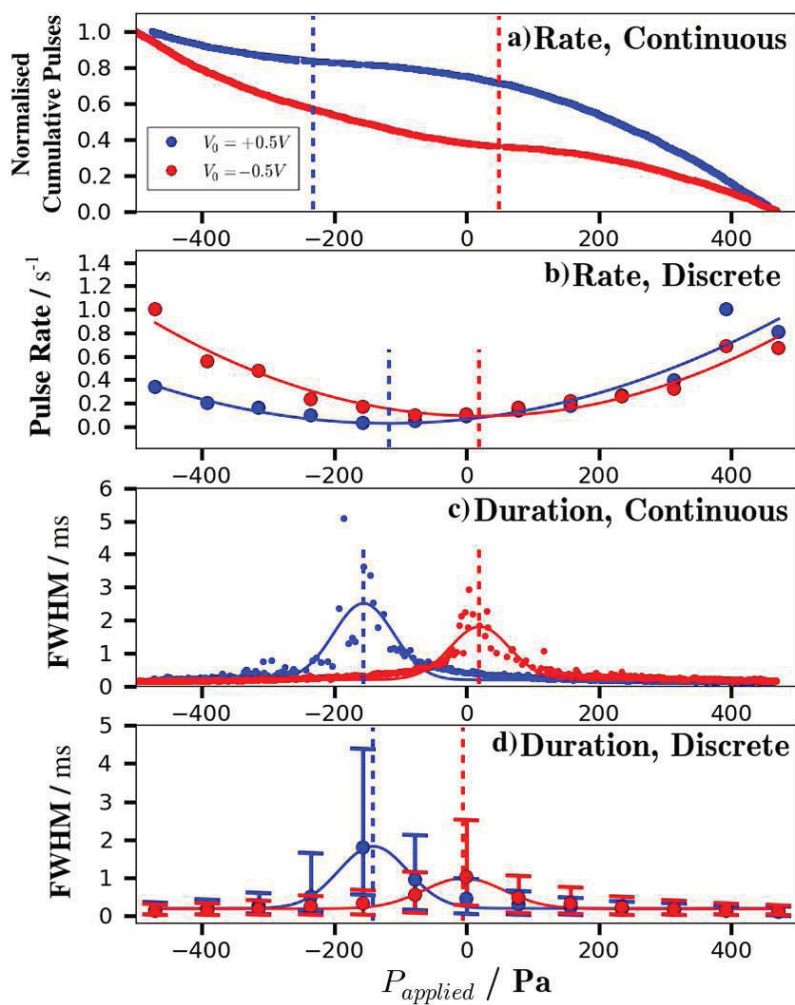
Figure 2: Indicative results for particle set C (Table 1), demonstrating analysis methods. Vertical dotted lines indicate derived values of P_0. (a) and (b) show data obtained from continuous and discrete particle rate measurements respectively. Cumulative data in (a) are normalized by the total pulse count in each run. (c) and (d) show data from continuous and discrete measurements of full width half maximum (FWHM) duration respectively. Each data point for 'discrete' cases is the average of at least 500 pulses. Error bars in (d) indicate the interquartile range around the median FWHM.

22
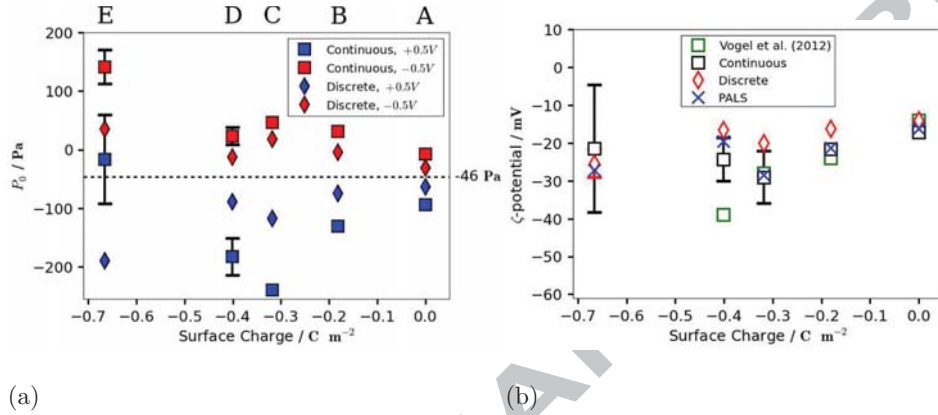
(a)   (b)

Figure 3: Data obtained using rate methods for particle sets A-E (Table 1). Particle set labels appear directly above the relevant data in (a), which plots applied pressure at minimum pulse rate (P_0) as a function of nominal surface charge density (σ). The horizontal black dotted line indicates $-P_{inherent}$. Error bars for continuous experiments indicate the range spanned in cases of increasing and decreasing pressure. (b) ζ-potentials calculated from the rate data. For continuous experiments, error bars indicate the standard deviation of four contributing data points; for discrete experiments, error bars indicate the range spanned by the two values at +0.5 V and -0.5 V (see Fig. 3(a)). Data from Vogel et al. [8] (green squares) were obtained using the continuous rate method. Mean values obtained using PALS are plotted in (b), with error bars (± 5 mV maximum) omitted for clarity. In both (a) and (b), error bars smaller than symbol size are omitted.
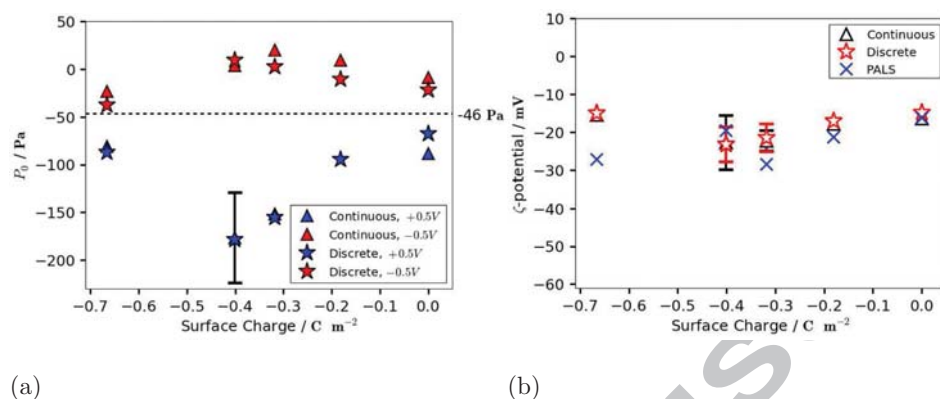
23

(a)   (b)

Figure 4: Data obtained using duration methods for particle sets A-E (Table 1). (a) Applied pressure at maximum pulse duration (P_0) as a function of nominal surface charge density (σ). (b) Corresponding ζ-potential data. Error bars and the horizontal black dotted line are as described for Fig. 3, with error bars for PALS (± 5 mV maximum) and those smaller than the symbol size omitted for clarity.
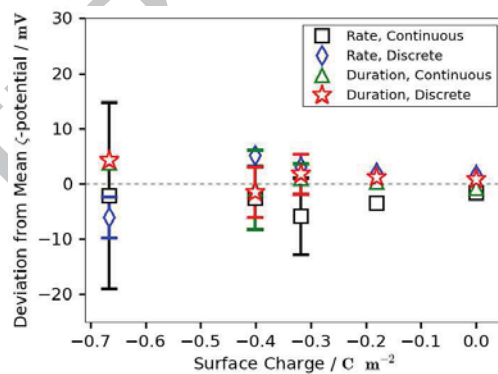

Figure 5: Summary of all ζ-potential data, plotted as a deviation from the mean over all methods for each particle set. Error bars correspond to those plotted in Figs. 3(b) and 4(b), and are omitted if smaller than the symbol size.
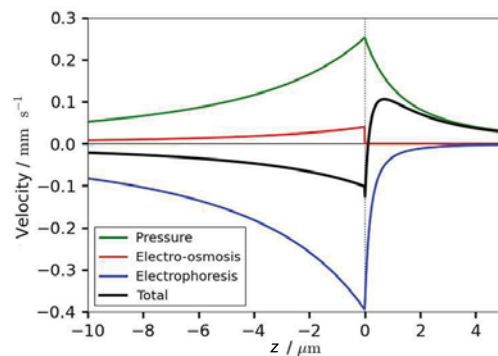
24

Figure 6: Example of simulated particle velocity components in which the direction of transport reverses at the pore constriction. The simulation is based on Eq. 1 using the following parameters: $P_{net} = -30$ Pa, $V_0 = 0.5$ V, particle radius 100 nm, $a = 450$ nm, $b = 46$ μm, $\zeta_{pore} = -12$ mV, $\zeta_{particle} = -30$ mV.
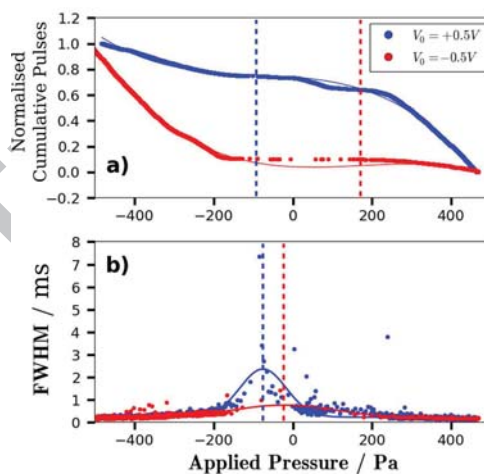

Figure 7: Example results using particle set E (Table 1). Vertical dotted lines indicate P_0, determined as described in Section 2.

25

References

[1] R. J. Hunter, Zeta Potential in Colloid Science: Principles and Applications, Academic Press, London, 1981.

[2] A. Delgado, F. Gonzalez-Caballero, R. Hunter, L. Koopal, J. Lyklema, Journal of Colloid and Interface Science 309 (2007) 194.

[3] A. S. Dukhin, P. J. Goetz, Ultrasound for Characterizing Colloids, Elsevier, Amsterdam, 2002.

[4] W. H. Coulter, US Patent 2,656,508, 1953.

[5] R. W. DeBlois, C. P. Bean, Journal of Colloid and Interface Science 61 (1977) 323.

[6] T. Ito, L. Sun, R. M. Crooks, Anal. Chem. 75 (2003) 2399.

[7] T. Ito, L. Sun, M. A. Bevan, R. M. Crooks, Langmuir 20 (2004) 6940.

[8] R. Vogel, W. Anderson, J. Eldridge, B. Glossop, G. Willmott, Analytical Chemistry (2012).

[9] J. A. Somerville, G. R. Willmott, J. Eldridge, M. Griffiths, K. M. McGrath, J. Coll. Interf. Sci. 394 (2013) 243.

[10] N. Arjmandi, W. V. Roy, L. Lagae, G. Borghs, Anal. Chem. 84 (2012) 8490.

[11] D. Kozak, W. Anderson, R. Vogel, S. Chen, F. Antaw, M. Trau, ACS Nano 6 (2012) 6990.

26

[12] G. Willmott, P. W. Moore, Nanotechnology 19 (2008) 475504.

[13] G. R. Willmott, R. Chaturvedi, S. J. W. Cummins, L. G. Groenewegen, Experimental Mechanics (2013) DOI: 10.1007/s11340–013–9795–5.

[14] G. Roberts, D. Kozak, W. Anderson, M. F. Broom, R. Vogel, M. Trau, Small 6 (2010) 2653.

[15] S. J. Sowerby, M. F. Broom, G. B. Petersen, Sensors and Actuators B 123 (2007) 325.

[16] A. H. Colby, Y. L. Colson, M. W. Grinstaff, Nanoscale 5 (2013) 3496.

[17] R. Vogel, G. Willmott, D. Kozak, G. Roberts, W. Anderson, L. Groenewgen, B. Glossop, A. Barnett, A. Turner, M. Trau, Analytical Chemistry 83 (2011) 3499.

[18] G. R. Willmott, R. Vogel, S. Yu, L. G. Groenewegen, G. Roberts, D. Kozak, W. Anderson, M. Trau, Journal of Physics: Condensed Matter 22 (2010) 454116.

[19] G. R. Willmott, B. E. T. Parry, Journal of Applied Physics 109 (2011) 094307.

[20] G. R. Willmott, M. Platt, G. U. Lee, Biomicrofluidics 6 (2012) 014103.

[21] M. A. Booth, R. Vogel, J. M. Curran, S. Harbison, J. Travas-Sejdic, Biosensors and Bioelectronics 45 (2013) 136.

[22] J. Parmentier, N. Thomas, A. Müllertz, G. Fricker, T. Rades, International Journal of Pharmaceutics 437 (2012) 253.

27

[23] L. Yang, M. F. Broom, I. G. Tucker, Pharmaceutical Research 29 (2012) 2578.

[24] E. van Bracht, R. Raavé, W. P. R. Verdurmen, R. G. Wismans, P. J. Geutjes, R. E. Brock, E. Oosterwijk, T. H. van Kuppevelt, W. F. Daamen, International Journal of Pharmaceutics 439 (2012) 127.

[25] G. S. Roberts, S. Yu, Q. Zeng, L. C. L. Chan, W. Anderson, A. H. Colby, M. W. Grinstaff, S. Reid, R. Vogel, Biosensors and Bioelectronics (2011).

[26] G. Bennett, R. Rajan, C. R. Bunt, M. A. Hussain, New Zealand Veterinary Journal 61 (2013) 119.

[27] D. Gazzola, S. C. Van Sluyter, A. Curioni, E. J. Waters, M. Marangon, Journal of Agricultural and Food Chemistry 60 (2012) 10666.

[28] Y. H. Ng, S. Rome, A. Jalabert, A. Forterre, H. Singh, C. L. Hincks, L. A. Salamonsen, PloS One 8 (2013) e58502.

[29] A. N. Böing, J. Stap, C. M. Hau, G. B. Afink, C. Ris-Stalpers, E. A. Reits, A. Sturk, C. J. F. van Noorden, R. Nieuwland, Biochimica et Biophysica Acta 1833 (2013) 1844.

[30] T. Katsuda, R. Tsuchiya, N. Kosaka, Y. Yoshioka, K. Takagaki, K. Oki, F. Takeshita, Y. Sakai, M. Kuroda, T. Ochiya, Scientific Reports 3 (2013) 1197.

[31] J. de Vrij, S. L. N. Maas, M. van Nispen, M. Sena-Esteves, R. W. A. Limpens, A. J. Koster, S. Leenstra, M. L. Lamfers, M. L. D. Broekman, Nanomedicine (2013) doi:10.2217/NNM.12.173.

[32] G. R. Willmott, M. G. Fisk, J. Eldridge, Biomicrofluidics 7 (2013) 064106.

[33] A. K. Yang, H. Lu, S. Y. Wu, H. C. Kwok, H. P. Ho, S. Yu, A. K. Cheung, S. K. Kong, Analytica Chimica Acta 782 (2013) 46.

[34] Y. S. Ang, L. Y. L. Yung, ACS Nano 6 (2012) 8815–8823.

[35] M. Low, S. Yu, M. Y. Han, X. Su, Aust. J. Chem. 64 (2011) 1229.

[36] S. R. German, L. Luo, H. S. White, T. L. Mega, J. Phys. Chem. C 117 (2013) 703.

[37] W. J. Lan, H. S. White, ACS Nano 6 (2012) 1757.

[38] E. Weatherall, G. R. Willmott, B. Glossop, Seventh International Conference on Sensing Technology (ICST) (2013) 874–878.

[39] Bangs Laboratories Inc. TechNote 206 9025, 2001.

[40] D. R. Lide, CRC Handbook of Chemistry and Physics, CRC Press, Boca Raton, 2005.

[41] J. H. L. Beal, A. Bubendorfer, T. Kemmitt, I. Hoek, W. M. Arnold, Biomicrofluidics 6 (2012) 036503.

[42] S. Devasenathipathy, J. G. Santiago, Micro- and Nano-Scale Diagnostic Techniques, Springer Verlag, New York, p. 121.

29

Graphical Abstract
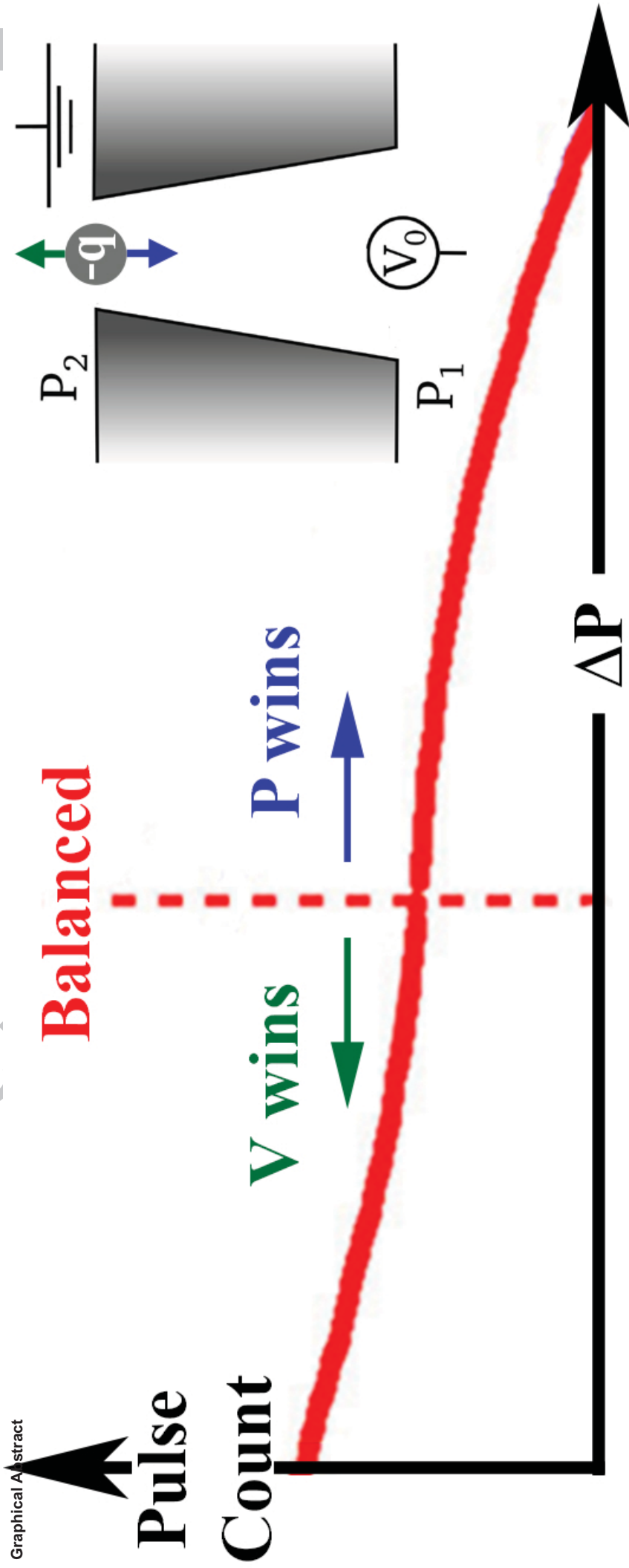
Highlights:

- 3 new ways to find zeta potentials using tunable resistive pulse sensing (TRPS).
- Comparative measurements using 5 particle sets, 4 TRPS methods and light scattering.
- Values and reproducibility are comparable to the standard light scattering method.
- Significantly developed assessment of uncertainty relative to previous TPRS work.